ACS Catalysis
Research Article
pubs.acs.org/acscatalysis

# Synergistic Catalysis between Pd and Fe in Gas Phase Hydrodeoxygenation of *m*-Cresol

Yongchun Hong,[†,‡,§] He Zhang,[†] Junming Sun,[†] Karim M. Ayman,[‡] Alyssa J. R. Hensley,[†] Meng Gu,[§] Mark H. Engelhard,[§] Jean-Sabin McEwen,[†,∥,⊥] and Yong Wang*[,†,‡]

[†]The Gene & Linda Voiland School of Chemical Engineering and Bioengineering, Washington State University, Pullman, Washington 99164, United States

[‡]Institute for Integrated Catalysis, Pacific Northwest National Laboratory, Richland, Washington 99352, United States

[§]Environmental Molecular Sciences Laboratory, Pacific Northwest National Laboratory, Richland, Washington 99352, United States

[∥]Department of Physics and Astronomy, Washington State University, Pullman, Washington 99164, United States

[⊥]Department of Chemistry, Washington State University, Pullman, Washington 99164, United States

*Supporting Information*

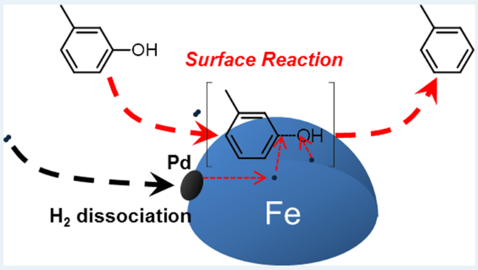

**ABSTRACT:** In this work, a series of $Pd/Fe_2O_3$ catalysts were synthesized, characterized, and evaluated for the hydrodeoxygenation (HDO) of *m*-cresol. It was found that the addition of Pd remarkably promotes the catalytic activity of Fe while the product distributions resemble that of monometallic Fe catalyst, showing high selectivity toward the production of toluene (C−O cleavage without saturation of aromatic ring and C−C cleavage). Reduced catalysts featured with Pd patches on the top of reduced Fe nanoparticle surface, and the interaction between Pd and Fe, was further confirmed using X-ray photoelectron spectroscopy (XPS), scanning transmission electron microscopy (STEM), and X-ray absorption near edge fine structure (XANES). A possible mechanism, including Pd assisted $H_2$ dissociation and Pd facilitated stabilization of the metallic Fe surface as well as Pd enhanced product desorption, is proposed to be responsible for the high activity and HDO selectivity in Pd−Fe catalysts. The synergic catalysis derived from Pd−Fe interaction found in this work was proved to be applicable to other precious metal promoted Fe catalysts, providing a promising strategy for future design of highly active and selective HDO catalysts.

**KEYWORDS:** *hydrodeoxygenation, biomass conversion, bimetallic catalysis, synergistic effects, iron catalyst, noble metal catalysis, $H_2$ sticking probability*

## 1. INTRODUCTION

The utilization of biomass as a renewable energy resource is the most promising approach to reduce the dependence on unrenewable fossil feedstock and the overall carbon footprint. One of the major technical obstacles in biofuel application is the high oxygen content in pyrolysis oil.[1] High oxygen content in liquid fuel leads to lower stability, lower heating value, and higher viscosity of fuel, which is not appreciable for current engine infrastructure.[2,3] Catalytic hydrodeoxygenation (HDO), in which the oxygen is removed in the form of water under a $H_2$ atmosphere, is proposed to be the most feasible technology to address this challenge.[4−6] Phenolic compounds such as guaiacol, cresol, and anisole were used as model compounds in the HDO research,[7,8] as they can be derived from pyrolysis of lignin, an abundant and nonedible organic carbon resource with less oxygen than cellulose and hemicellulose.

Several different types of catalysts have been intensively investigated in the HDO of phenolic compounds. Supported Co−Mo sulfide and Ni−Mo sulfide are commercial catalysts for hydrodesulphurization (HDS) and hydrodenitrogenation (HDN) processes in crude oil refineries[9,10] and thus have been considered as potential candidates for HDO. However, the performances of those catalysts are not satisfactory due to their relatively low activities in $H_2$ activation[11] and rapid deactivation with the sulfur stripping under S-"free" biomass feedstock.[12−14] To overcome those disadvantages, sulfur-free catalysts, such as noble metal and base metal catalysts were tested in HDO reactions.[15−20] For the noble metal catalysts, their negligible barriers for $H_2$ dissociation enables atmospheric operation,[21,22] while their high C−C bond cleavage rates often lead to the saturation of aromatic rings and the further deconstruction of C−C backbones.[20,23,24] In addition, the high cost of noble metals limits their application. The much cheaper base metal catalysts usually show relatively lower activity than noble metal catalysts; however, their unique selectivity toward C−O cleavage makes them the preferred candidates for HDO application.[19,20] For example, Dufour et al.[18,19,25,26] explored Fe-based catalysts ($Fe/SiO_2$ and Fe/C) in the HDO of guaiacol and pyrolysis oil and found that the Fe catalysts show promising selectivity toward the formation of aromatics (mainly

**Received:** April 29, 2014
**Revised:** July 21, 2014
**Published:** July 29, 2014

dx.doi.org/10.1021/cs500578g | *ACS Catal.* 2014, 4, 3335−3345

benzene, toluene, and xylene, i.e., BTX). In our previous study, the catalytic behaviors for guaiacol HDO on noble and base metal catalysts were compared.[20] The noble metal catalysts, like Ru/C and Pd/C, showed significant C−C bond cleavage selectivity, while the base metal catalysts, like Cu/C and Fe/C, showed higher C−O bond cleavage selectivity and relatively lower activity. However, the combination of base metal (Fe) with noble metal (Pd) led to a dramatic increase in the activity of guaiacol HDO and benzene yield (∼80%), suggesting a synergy in Pd−Fe bimetallic catalysts.[20]

In this work, the synergic effect between Pd and Fe was studied on Pd-promoted Fe nanoparticles, which eliminates the influence of catalyst supports. A combination of advanced characterizations was used to understand the structure of the Pd−Fe catalysts. To elucidate the synergic effect between Pd and Fe with minimum complications in the reaction network, *m*-cresol was chosen as a substrate as it is the simplest compound with all functional groups of interest (Ar−OH and Ar−$CH_3$). A distinct synergic effect was found in the HDO of *m*-cresol, and a mechanism was proposed based on the specific roles of Pd and Fe in the synergic catalysis. The synergistic effects were also found for other precious metal promoted Fe catalysts including Pt−Fe, Ru−Fe, and Rh−Fe.

## 2. EXPERIMENTAL SECTION

**2.1. Preparation of $Fe_2O_3$ Support.** $Fe_2O_3$ support was prepared by an aqueous phase precipitation of ferric nitrate ($Fe(NO_3)_3{\cdot}9H_2O$, Sigma-Aldrich, ≥99.999%) with ammonium carbonate ($(NH_4)_2CO_3$, Sigma-Aldrich, 99.999%) at room temperature, and the pH of the resulting solution was kept constant at approximately 8.[27] The precipitate was collected via filtration and then washed with excessive deionized water six times. The obtained solids were dried in an oven (80 °C) overnight, crushed and sieved to 60−100 mesh, and then calcined in an oven at 400 °C for 5 h.

**2.2. Preparation of $Pd/Fe_2O_3$, $Pt/Fe_2O_3$, $Ru/Fe_2O_3$, and $Rh/Fe_2O_3$ Samples.** $Pd/Fe_2O_3$ samples with different Pd loadings (0.1−5 wt %) were prepared using incipient wetness impregnation.[20] In a typical synthesis process, $Pd(NH_3)_4(NO_3)_2$ aqueous solution (Sigma-Aldrich, 10 wt % solution with 99.99% metal based purity) was diluted to a certain concentration (0.1 M for 5 wt % sample) with deionized water and then added onto the as-prepared $Fe_2O_3$ powder. After impregnation, the resulting samples were dried in an oven (80 °C) overnight, crushed and sieved to 60−100 mesh, and then calcined in flowing $N_2$ (50 mL/min, STP) at 350 °C (ramping rate = 5 °C/min) for 2 h. The resulting samples were denoted as *m*$Pd/Fe_2O_3$, with *m* indicating the loading of Pd.

$Pt/Fe_2O_3$, $Ru/Fe_2O_3$, and $Rh/Fe_2O_3$ samples were synthesized using a similar incipient wetness impregnation method to that for the $Pd/Fe_2O_3$ samples. Precursors ($Pt(NH_3)_4(NO_3)_2$, Aldrich, 99.995%; $RuCl_3$, Sigma-Aldrich, 46.1 wt % Ru; $RhCl_3{\cdot}H_2O$, Aldrich, 38−40 wt % Rh) were dissolved in deionized water and then added onto the as-prepared $Fe_2O_3$ powder. The postsynthetic procedure for those samples was the same as that of $Pd/Fe_2O_3$ samples described above. The metal loading for all samples was kept at 1 wt %, and the catalysts were denoted as $1Pt/Fe_2O_3$, $1Ru/Fe_2O_3$, and $1Rh/Fe_2O_3$.

**2.3. Preparation of 5Pd/C Catalyst.** Pd/C catalyst with 5 wt % Pd loading (denoted as 5Pd/C) was prepared by incipient wetness impregnation.[20] A desired amount of $Pd(NH_3)_4(NO_3)_2$ (Sigma-Aldrich, 99.99%) aqueous solution was added to a TA70 carbon (1290 $m^2$ $g^{-1}$, Pico Inc.) support. After impregnation, the resulting catalyst was dried in an oven (80 °C) overnight and then calcined in flowing $N_2$ (50 mL/min, STP) at 350 °C (ramping rate = 5 °C/min) for 2 h.

**2.4. Characterizations.** Transmission electron microscopic (TEM) images were collected on a Philips CM-200 platform operated at 200 kV. Samples were dispersed in ethanol under ultrasonic agitation before loading on the support grids.

Aberration corrected high angle annular dark field scanning transmission electron microscopy (AC-HAADF-STEM) was performed with an FEI Titan 80−300 operated at 300 kV. The FEI Titan is equipped with a CEOS GmbH double-hexapole aberration corrector for the probe-forming lens, which allows imaging at a resolution of ∼0.1 nm in STEM mode. The images were acquired in HAADF mode with an inner collection angle of 52 mrad. The STEM sample preparation involved the mounting of powder samples on copper grids covered lacey carbon support film and loading into the microscope. $1Pd/Fe_2O_3$ samples were subjected to a reduction-passivation process prior to STEM characterizations. The reduction-passivation process was conducted in the following manner: the sample was first reduced in flowing 50 vol % $H_2$ (balanced with $N_2$, 50 mL/min, STP) at 300 °C (ramping rate = 5 °C/min) for 2 h, cooled to room temperature in a $H_2$ atmosphere, and then purged overnight with flowing passivation gas (1 vol % $O_2$ in $N_2$, 10 mL/min, STP). The spent $1Pd/Fe_2O_3$ samples were recovered after a typical catalytic test with a time-on-stream (TOS) of 12 h and subjected to the sample preparation process of STEM without any pretreatment.

X-ray diffraction (XRD) patterns were collected on a Philips X'pert MPD (Model PW 3040/00) equipped with a Cu K$\alpha$ (incident wavelength $\lambda$ = 0.15406 nm) X-ray source operating at 40 kV and 50 mA. A step-size of 0.04° and accumulation time of 1.6 s were used during the scanning. The obtained patterns were analyzed using the MDI Jade 6 software with Joint Committee on Powder Diffraction Standards (JCPDS) cards.

*In situ* XRD studies were performed at the National Synchrotron Light Source (NSLS, beamline X-18A) of Brookhaven National Laboratory (BNL). A total of 5 mg of catalyst was diluted with 10 mg of carbon and packed into a 1/8″ glassy carbon reactor tube. The reactor was then loaded into an in-house built stainless steel cell, heated with resistive cartridge heaters; the setup details have been previously reported.[28] The $1Pd/Fe_2O_3$ sample was *in situ* reduced under 50 vol % $H_2$ (50 mL/min, STP, balanced with Ar) at 300 °C with a ramp rate = 5 °C/min; XRD (incident beam energy =12.4 keV) data were collected by a CCD area detector at different reduction temperatures and/or durations, with an acquisition time of ∼20 s. The background pattern for the blank reactor with carbon was collected and subtracted accordingly. For comparison purposes, the diffraction angle ($\theta$) was corrected to that at 8.04 keV (Cu K$\alpha$ line), which is commonly adapted in the literature, using Bragg's equation.[29]

Temperature-programmed reduction (TPR) and desorption (TPD) were conducted on a homemade system conjugated with a mass spectrometer (Omnistar gas analyzer GSD 301). Before the TPR and TPD tests, 50 mg of sample was loaded into a 1/8″ quartz tube and reduced at 300 °C for 2 h in flowing 50 vol % $H_2$ (50 mL/min, STP, balanced with He). For TPR tests, the reduced samples were further treated by steam (introduced by passing 50 vol % $H_2$ though a bubbler filled with DI water at room temperature) at 300 °C for another 2 h, then purged with He (50 mL/min, STP) for 30 min, followed by cooling down to room temperature in an inert atmosphere. The TPR test was conducted in flowing 5 vol % $H_2$ balanced by He (50 mL/min, STP) with a ramp rate of 10 °C/min. For TPD tests, the reduced samples were first purged with He (50 mL/min, STP) for 30 min after reduction and then cooled down to the desired temperature for adsorption ($H_2$, room temperature; toluene, 110 °C). After adsorption for 30 min (high purity $H_2$ was introduced at a flow rate of 50 mL/min (STP), while toluene was introduced by passing He though a bubbler filled with toluene at room temperature), the system was purged with He for another 30 min, and the TPD test was conducted in flowing He (50 mL/min, STP) with a ramping rate of 15 °C/min. The effluent for each test was analyzed with an online mass spectrometer.

Pseudo-*in situ* X-ray photoelectron spectroscopy (XPS) measurements of Pd/$Fe_2O_3$ samples were performed on a Physical Electronics Quantum 2000 Scanning ESCA microprobe equipped with a focused monochromatic Al K$\alpha$ X-ray (1486.7 eV) source, a spherical section analyzer, and an attached catalytic side chamber. After the collection of XPS spectra, fresh samples were transferred to the catalytic side chamber and reduced under 50 vol % $H_2$ (50 mL/min, STP, balanced with Ar) at 300 °C (ramp rate = 5 °C/min) for 2 h before cooling to room temperature and then transferred back to the main chamber for measuring photoelectron energy spectra. The binding energy values are referenced to the contamination carbon (C 1s) at 285.00 eV.

*In situ* X-ray absorption near edge structure (XANES) measurements were performed in the same setup described above for *in situ* XRD studies. The 1Pd/$Fe_2O_3$ sample was *in situ* reduced under 50 vol % $H_2$ (50 mL/min (STP) balanced with Ar) at 300 °C for 2 h (ramp rate = 5 °C/min) before being subjected to steam treatment. Steam treatment was carried out at 300 °C for ~30 min. Steam was introduced by bubbling $H_2$ gas (50 mL/min, STP) though a sealed container with deionized water at room temperature (water partial pressure = 2.3 kPa or 2.3 vol %). The container was prepurged with $H_2$ before being switched to feed the reactor. XANES data were collected in transmission mode with an Fe foil spectrum collected simultaneously with each scan. XANES data processing and the analyses were performed using the Athena program of the IFEFFIT data analysis package.[30,31]

**2.5. Catalytic Activity Measurements.** Catalyst activity measurements for HDO of *m*-cresol were performed in a stainless steel fixed-bed reactor. In a typical procedure, 100 mg of sample (60−100 mesh) was loaded with quartz wool layers at both ends. Before the reaction, catalysts were first reduced in 50 vol % $H_2$ (balanced with $N_2$, 50 mL/min (STP)) at 300 °C with a ramping rate of 5 °C/min for 2 h, followed by purging with $N_2$ for 30 min. The HDO reaction was then initiated by introducing reactant gas (0.45 vol % *m*-cresol and 40 vol % $H_2$, balanced with $N_2$, 40 mL/min (STP)) into the reactor at 300 °C. The reactant gas was obtained by mixing 40 vol %$H_2$ (balanced with $N_2$, 40 mL/min, STP) gas with *m*-cresol (99%, Sigma-Aldrich, fed by a Core Parmer 74900 syringe pump at pumping rate = 0.05 mL/h) in a vaporizer (190 °C). Both the reactor inlet and outlet were heated to above 190 °C to avoid the condensation of liquid products. The products were analyzed by an online Shimadzu 2400 Gas Chromatography (GC) equipped with an autosampling valve, RTX (30 m, 0.53 mm, 0.5 $\mu$m) column, and Flame Ionization Detector (FID). The bypassed products were cooled in a cold trap, and the gaseous products were sent to an online Agilent 3000A Micro GC for the analysis of gas products (i.e., $CH_4$, $CO_2$, CO, and $C_2H_6$). The product selectivity and yield were calculated on a carbon basis.

The effect of both external and internal mass transfer limitation was negligible under the testing conditions as further increasing flow rate (at constant GHSV) or reducing pallet size did not affect the conversion (Figure S1 in Supporting Information).

**2.6. Computational Details.** Density functional theory (DFT) calculations were performed to study the adsorption of a hydrogen atom on an Fe (110) surface with a single Pd impurity using the Vienna *Ab Initio* Simulation Package (VASP) code,[32,33] and all the calculation details were the same as those presented in the paper by Sun et al.[20] The model surface studied here was an Fe (110) surface with a single Pd impurity in the top layer. The Fe (110) facet was chosen because it is the closest packed facet in the bcc Fe lattice.[34] The segregation of Pd to the surface in an Fe host was determined to be the most favorable configuration of this system by Sun et al.[20] and Ruban et al.[35,36] Also, as Pd has a lower surface energy than Fe, the presence of Pd in the surface is expected.[37] The lattice constant of Fe was determined theoretically by minimizing the total energy of the Fe bcc unit cell. This resulted in an Fe lattice constant of 2.827 Å. This result agrees well with other theoretical results and the experimental values.[38] The surface was modeled using a p(4 × 4) supercell with four substrate layers and the repeating surfaces were separated by ~12 Å of vacuum. The bottom two layers were kept fixed in their bulk positions, and all other atoms were allowed to relax, including the adsorbate.

Numerous adsorption sites were examined, and each site was evaluated using the adsorption energy. This was calculated as the difference in the energy of the molecule adsorbed on the surface and the energy of the individual surface and adsorbate molecule according to

$$E_{\mathrm{ads}} = E_{\mathrm{Surface+H}} - \frac{1}{2}E_{\mathrm{H_2}} - E_{\mathrm{Surface}} \qquad (1)$$

With this definition, a favorable adsorption will occur when the adsorption energy is negative.

## 3. RESULT AND DISCUSSION

**3.1. Structure of Pd/$Fe_2O_3$ Samples.** In our previous work,[20] carbon supported Pd−Fe bimetallic catalysts were synthesized using a sequential incipient wetness impregnation method. The catalysts synthesized showed a bimodal distribution with both small (1−5 nm) and large nanoparticles (20−100 nm).[20] Such inhomogeneity in size and morphology prevents the identification of the catalytic active sites or understanding of the synergic effect between Pd and Fe. In this work, to eliminate the possible complications of varying Pd−Fe particle sizes and the carbon support effects on HDO activity, Pd/$Fe_2O_3$ catalysts were synthesized by impregnating a Pd precursor solution onto the surface of as-prepared $Fe_2O_3$ nanoparticles without using a support such as activated carbon. The as-prepared $Fe_2O_3$ nanoparticles have a relatively uniform particle size of 20 nm in diameter and a surface area of 40 $m^2$/g, and the addition of Pd has negligible effects on the texture properties of $Fe_2O_3$ nanoparticles.[39]

As shown in Figure 1, the fresh 5Pd/$Fe_2O_3$ sample consists of Pd entities (ca. 5 nm) attached to the surface of iron oxide nanoparticles, *i.e*, the Pd-on-$Fe_2O_3$ structure as expected. Both the iron oxide nanoparticle and Pd entity are in nearly spherical

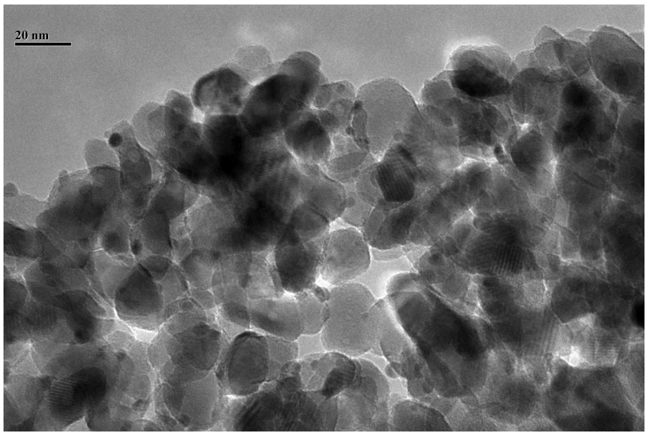

**Figure 1.** Representative TEM (accelerating voltage = 200 kV) images for 5Pd/$Fe_2O_3$ sample. The dark patches show the location of Pd on the sample.

shape. XRD characterizations (Figure 2) indicate that the iron oxide nanoparticles are present as $\alpha$-hematite ($\alpha$-$Fe_2O_3$, JCPDS card no.: 33-0664), and Pd entities are metallic Pd (JCPDS card no.: 46-1043).

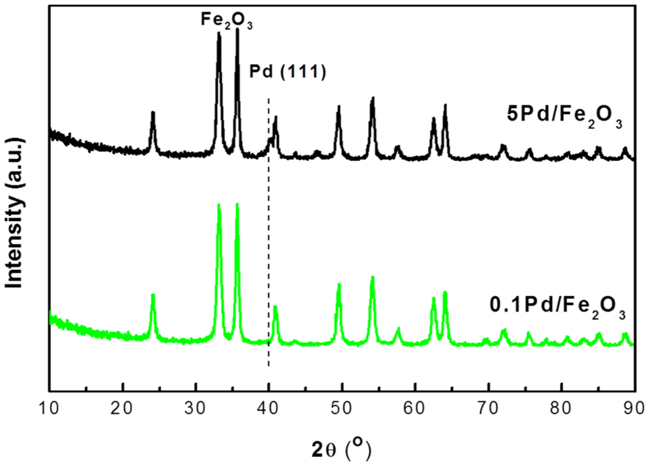

**Figure 2.** XRD patterns of fresh *m*Pd/$Fe_2O_3$ samples measured with Cu K$\alpha$ source operated at 40 kV and 50 mA.

As shown in Figure 2, the addition of Pd did not significantly change the crystallographic characteristics of the $Fe_2O_3$ nanoparticles. The positions and relative intensities of the diffraction peaks of $Fe_2O_3$ do not change with increasing Pd loading. The average crystal size of $Fe_2O_3$, calculated based on the Scherrer equation,[40] is 15.8 nm, which is very close to the particle size obtained from TEM (about 20 nm shown in Figure 1).

While at low Pd loadings (<5 wt %) the diffraction peak for the Pd (111) plane is nearly absent, a small peak at about 40° was detected for the 5Pd/$Fe_2O_3$ sample. The absence of the Pd characteristics for the 1Pd/$Fe_2O_3$[39] and 0.1Pd/$Fe_2O_3$ samples suggests that the Pd entities in both samples are highly dispersed or below the detection limit of XRD. On the basis of the TEM and XRD characterizations, unreduced Pd/$Fe_2O_3$ samples have Pd entities that are <5 nm in diameter attached on the surface of $Fe_2O_3$ nanoparticles with diameters of 20 nm.

The evolution of Fe species was further investigated using *in situ* XRD. Figure 3 shows the XRD patterns for the 1Pd/$Fe_2O_3$ sample at different reduction temperatures (pattern recorded when the temperature was reached with 5 °C/min ramping rate). The diffraction pattern for the 1Pd/$Fe_2O_3$ sample reduced for 30 min at 300 °C is also included in Figure 3. The XRD pattern for the fresh 1Pd/$Fe_2O_3$ sample shows the $\alpha$-hematite phase of $Fe_2O_3$ and absence of the Pd diffraction peak, which is consistent with results reported using regular XRD.[39] The pattern remains unchanged at reduction temperatures of 100 and 200 °C, while a significant transformation occurs when the temperature reaches 300 °C; namely, the disappearance of the $\alpha$-hematite phase and formation of the magnetite phase ($Fe_3O_4$). An even more drastic transformation can be observed while the sample was held at 300 °C for 30 min, where nearly the full reduction of the magnetite phase is evidenced by the disappearance of the diffraction peaks of magnetite and the simultaneous appearance of the diffraction peaks of metallic Fe. However, XRD is not a surface sensitive technique and thus can only provide limited information on the surface structure of a reduced sample.

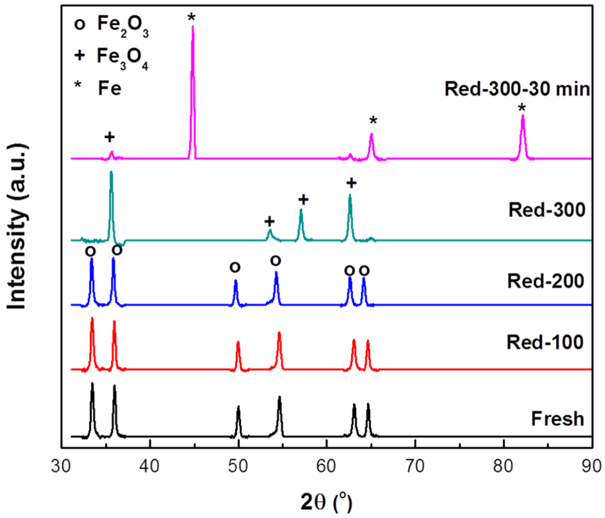

**Figure 3.** *In situ* XRD patterns for fresh and reduced (under 50 vol % $H_2$ (50 mL/min, STP, balanced with Ar)) 1Pd/$Fe_2O_3$ samples measured with incident beam energy = 12.4 keV. The spectrum is corrected to that at 8.04 keV (Cu K$\alpha$ line) using Bragg's equation.

The morphologies of the reduced and spent 1Pd/$Fe_2O_3$ catalyst were further investigated using AC-HAADF-STEM. Figure 4 shows the representative STEM images for the reduced (Figure 4a) and spent (Figure 4b) 1Pd/$Fe_2O_3$ catalysts. The Z contrast STEM images enable differentiating Pd from Fe atoms. The bright islands with a diameter of 1−2 nm are Pd entities on the surface of Fe, while the darker spots underneath those islands are Fe atoms. The negligible difference in morphology between the reduced and spent catalysts suggests that the Pd−Fe structure is robust under reaction conditions. The atomic resolution image (Figure 4a2) of Pd entities shows 3D structures, while Figure 4a3 and b3 suggest a 2D-like flat structure of Pd on the Fe surface. This Pd-on-Fe structure was similar to the Pd−Fe structure found in the Pd−Fe/C catalyst previously reported.[20]

To provide better understanding of the surface structure of the Pd−Fe catalyst, its surface element composition as well as electron structure was measured with *pseudo-in situ* XPS characterization. The surface compositions of fresh and reduced $Fe_2O_3$ and Pd/$Fe_2O_3$ samples are summarized in Table 1. Apparently, reduction treatment significantly reduced $Fe_2O_3$ as

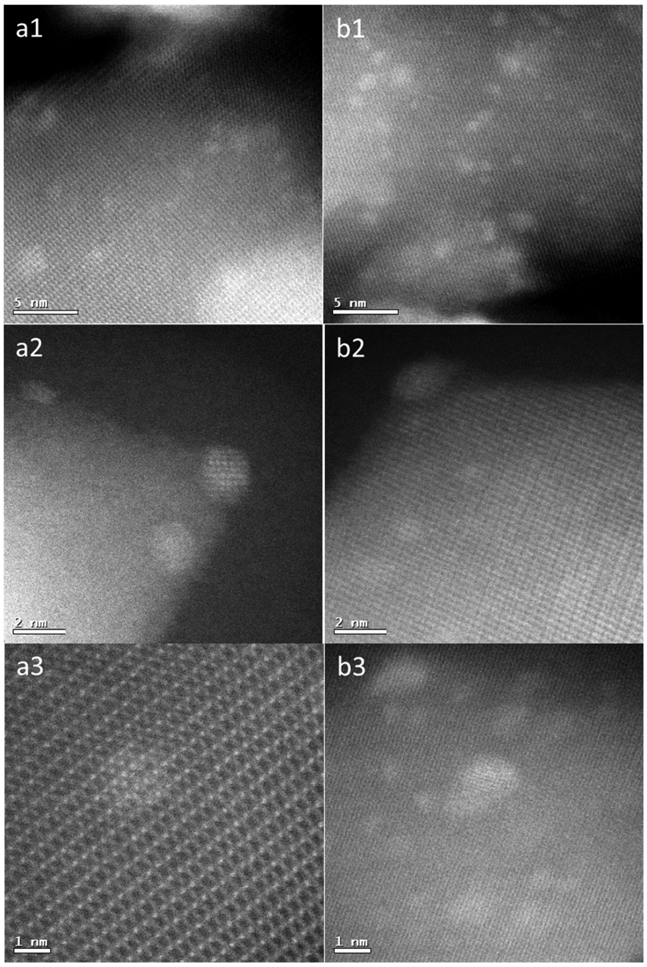

**Figure 4.** Representative AC-HAADF-STEM (accelerating voltage = 300 kV) images for reduced (left column, reduced under a 50 vol % $H_2$ (50 mL/min, STP, balanced with $N_2$) at 300 °C (ramp rate = 5 °C/min) for 5 h and passivated in flowing 1 vol % $O_2$ (10 mL/min, STP, balanced with $N_2$) at room temperature for 12 h) and spent (right column, subjected to a typical reaction condition (catalyst loading = 100 mg; pretreated in flowing 50 vol % $H_2$ (50 mL/min, STP, balanced with $N_2$) at 300 °C (ramp rate = 5 °C/min) for 2 h; reaction temperature = 300 °C; reaction gas = 0.45 vol % *m*-cresol and 40 vol % $H_2$, balanced with $N_2$, 40 mL/min (STP); GHSV = 24 000 $h^{-1}$) for 12 h and passivated in flowing 1 vol % $O_2$ (10 mL/min, STP, balanced with $N_2$) at room temperature for 12 h) 1Pd/$Fe_2O_3$ samples. Brighter dots show the location of Pd atoms while darker dots show that of Fe atoms.

**Table 1. Surface Atomic Composition of Fresh and Reduced Pd/$Fe_2O_3$ Samples**

| sample | treatment | O (%) | Fe (%) | Pd (%) | Pd/Fe |
|---|---|---|---|---|---|
| 0.1Pd/$Fe_2O_3$ | fresh | 41.9 | 54.8 | 0.08 | 0.001 |
| | reduced | 7.80 | 89.1 | 0.10 | 0.001 |
| 1Pd/$Fe_2O_3$ | fresh | 42.0 | 53.4 | 0.39 | 0.007 |
| | reduced | 5.60 | 90.3 | 1.74 | 0.019 |
| 5Pd/$Fe_2O_3$ | fresh | 41.0 | 54.2 | 1.00 | 0.018 |
| | reduced | 7.00 | 82.1 | 3.26 | 0.039 |
| $Fe_2O_3$ | fresh | 40.8 | 54.5 | | |
| | reduced | 7.00 | 86.8 | | |

evidenced by the reduction of oxygen content from about 42% to about 7% with the concurrent increase in the Fe composition from about 54% to about 80–90%. More importantly, the surface Pd/Fe ratio increased remarkably after reduction, suggesting the surface enrichment in Pd. This phenomenon is consistent with the DFT calculations[20,41] and studies on a model system.[42] Given the fact that the surface Pd/Fe ratio (*ca* 1:50 for 1Pd/$Fe_2O_3$, Table 1) is much lower than the estimated surface coverage of Pd assuming a Pd monolayer covering of Fe (0.2 ML for 1Pd/$Fe_2O_3$), the majority of the Pd entities should be featured as 3D nanoparticles attached to the Fe surface.

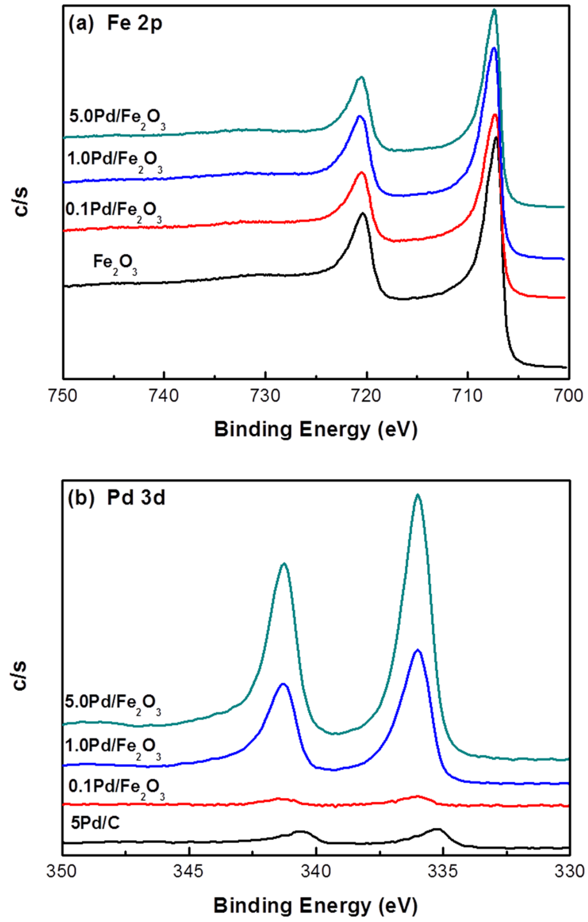

**Figure 5.** Pseudo-*in situ* XPS spectra of reduced (under 50 vol % $H_2$ (50 mL/min, STP, balanced with Ar) at 300 °C (ramp rate = 5 °C/min) for 2 h) Pd/$Fe_2O_3$ samples in the Fe 2p (a) and Pd 3d (b) regions mesured with an Al K*α* X-ray (1486.7 eV) source. The binding energy values are referenced to the contamination carbon (C 1s) at 285.00 eV.

The detailed XPS spectra for *in situ* reduced $Fe_2O_3$ and Pd/$Fe_2O_3$ samples at Fe 2p and Pd 3d regions are shown in Figure 5, which can be used to help understand the potential interaction between Fe and Pd. The binding energy for Fe $2p_{3/2}$ (707.5 eV) is consistent with the position of metallic Fe,[43] suggesting near full reduction of the surface Fe. Trace amounts of surface oxide species cannot be excluded, due to the asymmetric features of the Fe 2p peaks at the high binding energy side as well as the presence of <10% coverage of oxygen on the surface (Table 1). Interestingly, the binding energy for Pd $3d_{5/2}$ in reduced samples (336.0 eV) shows a significant blue shift, compared with that in the 5Pd/C reference sample (335.2 eV), which is consistent with the position for metallic Pd (335.1 eV).[44] Tsang et al.[45] reported similar phenomena in the annealing of the Pd/$Fe_2O_3$ catalyst (prepared via coprecipitation) at 195 °C where the Pd $3d_{5/2}$ peak showed a remarkable blue shift (ca. 1.0 eV) while the Fe $2p_{3/2}$ peak simultaneously showed a red shift of ca. 1.0 eV. The observed simultaneous shift or core-level electron binding energy of Pd and Fe can be attributed to the electron transfer from Pd to Fe, as suggested in earlier literature.[42,46] The absence of the noticeable shift in Fe 2p electron binding energy in this study could be due to the low Pd/Fe ratio on the surface (Table 1); i.e., the signal from Fe atoms in close contact with Pd could be buried by the large population of Fe atoms which are not directly associated with Pd, leading to the negligible change in XPS spectra.

Based on the AC-HAADF-STEM, XRD, and XPS results discussed above, the Pd−Fe catalyst after reduction has the Pd-on-Fe structures (Pd entities are present in either 3D clusters or 2D flakes on metallic Fe surface) with evident electronic interaction between Pd and Fe.

### 3.2. Catalytic Performance in *m*-Cresol HDO.

In this work, the activity of Fe, Pd, and other precious metal promoted Fe catalysts was studied in the HDO of *m*-cresol, one of the important lignin derivatives. A simplified reaction network is shown in Scheme 1. There are three major reaction pathways for HDO of *m*-cresol: (1) direct hydrogenolysis of Ar−OH bond to form toluene and its methyl-transfer derivatives (benzene and xylene), (2) Ar−C bond cleavage to form phenol and its derivatives (benzene, cyclohexanone, etc.), and (3) aromatic ring saturation to form methyl-cyclohexanone and its derivatives (methyl-cyclohexnol etc.). Another major side reaction is the further breakdown of the above products to $C_1$−$C_2$ hydrocarbons under severe conditions, as reported over Co and Ru catalysts.[19,20]

**Scheme 1. Reaction Network for HDO of *m*-Cresol**

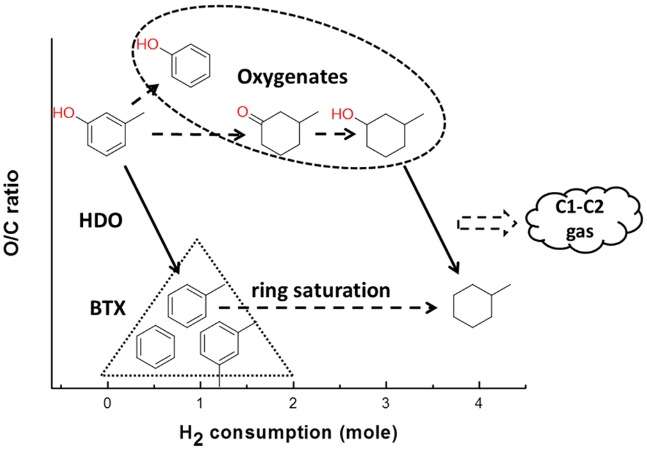

To achieve a better atom economy of C and H, catalysts should be selective to the production of toluene and its derivatives (BTX) while minimizing ring saturation, which consumes extra $H_2$ without lowering the oxygen/carbon ratio. Although the saturation of aromatics in fuel to produce cycloalkanes is motivated to reduce the environmental consequences of aromatics combustion,[47,48] the endothermic nature of the hydrogenation reaction makes it energetically undesirable.

Figure 6 summarizes the catalytic performances of Pd/$Fe_2O_3$ catalysts. For comparison purposes, the performances of $Fe_2O_3$ and 5Pd/C are also included. The monometallic Fe catalyst showed a *m*-cresol conversion of ca. 20% with high selectivity (ca. 90%) toward the formation of BTX (mainly toluene, >80%), while the 5Pd/C reference catalyst showed a lower conversion of *m*-cresol (10%) with 18% selectivity to oxygenates (i.e., cyclohexanol and cyclohexanone), due to the aromatic ring saturation. On the other hand, the combination of Pd and Fe showed a remarkable synergic effect, leading to a higher *m*-cresol conversion (1.5-fold at 0.1 wt % and 2-fold at 5 wt % Pd loading compared with monometallic Fe catalyst) while maintaining high selectivity to BTX (>90%) as that of Fe.

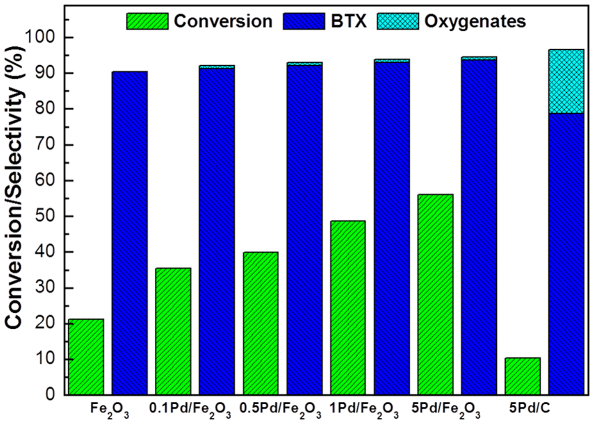

**Figure 6.** Catalytic performances of $Fe_2O_3$, *m*Pd/$Fe_2O_3$, and 5Pd/C catalysts for *m*-cresol HDO at 300 °C. Catalyst loading = 100 mg; pretreated in flowing 50 vol % $H_2$ (50 mL/min, STP, balanced with $N_2$) at 300 °C (ramp rate = 5 °C/min) for 2 h; reaction gas = 0.45 vol % *m*-cresol and 40 vol % $H_2$, balanced with $N_2$, 40 mL/min (STP); GHSV = 24 000 $h^{-1}$.

Our previous theoretical calculations[20] suggested that Fe is the active phase for the adsorption and activation of phenolic compounds, as the phenolic compounds were preferentially adsorbed on Fe sites with a noticeable distortion of the C−O bond. In addition, the doping of Pd on the Fe surface significantly reduced the adsorption energy of aromatic products (e.g., benzene), which is believed to be related to the higher activity and lower selectivity to C1−C2 products on Pd−Fe for guaiacol HDO.[41]

In this work, the high selectivity toward toluene production over the fully reduced Fe surface in the *m*-cresol HDO reaction gives conclusive proof of the selective C−O activation of Fe in HDO catalysis, without the complexity of a complex reaction network (e.g., guaiacol) and support effects. A similar product selectivity between the Fe and Pd−Fe catalysts suggests that the Fe serves as the catalytically active sites in the Pd−Fe catalysts. The roles of Pd in the synergic catalysis could include the potential stabilization of the Fe surface, weakened product desorption as suggested by the DFT calculations,[41] or promoted hydrogen activation by Pd.

To make a rigorous comparison of the catalyst activity, the reaction rates were obtained on the basis of data collected at low conversion levels (8−10%). In addition, mass specific activities (MSAs) were calculated by normalizing the reaction rate ($\mu$mol/s) to the total amount of catalyst. As references, the MSAs based on Fe ($MSA_{Fe}$), Pd ($MSA_{Pd}$), and their linear combination ($MSA_{linear}$, assuming Fe and Pd in Pd/$Fe_2O_3$ samples have the same MSAs as their monometallic counterparts and the overall activity of Pd/$Fe_2O_3$ is the linear combination of both metals, i.e., the nonsynergic scenario) were also calculated and are listed in Table 2. The Pd/$Fe_2O_3$ samples showed high BTX selectivity (>80%) and almost no oxygenates formation (products from aromatic ring saturation).

Table 2. Mass Specific Activities for $Pd/Fe_2O_3$, $Fe_2O_3$ and 5Pd/C Samples

| sample | GHSV ($h^{-1}$) | conv. (%) | BTX/Oxy (%/%) | $MSA_{cat}$ | $MSA_{Fe}$ | $MSA_{Pd}$ | $MSA_{linear}$ |
|---|---|---|---|---|---|---|---|
| $5Pd/Fe_2O_3$ | 96 000 | 10 | 87/<1[a] | 0.54[b] | 0.72[c] | 10.58[d] | 0.38[e] |
| $1Pd/Fe_2O_3$ | 96 000 | 9.4 | 89/<1 | 0.50 | 0.70 | 49.74 | 0.29 |
| $0.1Pd/Fe_2O_3$ | 96 000 | 8.9 | 91/<1 | 0.47 | 0.67 | 470.94 | 0.27 |
| $Fe_2O_3$ | 48 000 | 10 | 92/<1 | 0.26 | 0.38 | | |
| 5Pd/C | 24 000 | 10 | 79/18 | 0.13 | | 2.65 | |

[a] BTX selectivity/oxygenates selectivity. [b] MSA based on total catalyst weight ($\mu$mol/s/$g_{cat}$) = reaction rate ($\mu$mol/s)/catalyst weight ($g_{cat}$). [c] MSA based on Fe loading ($\mu$mol/s/$g_{Fe}$) = reaction rate ($\mu$mol/s)/Fe loading ($g_{Fe}$). [d] MSA based on Pd loading ($\mu$mol/s/$g_{Pd}$) = reaction rate ($\mu$mol/s)/Pd loading ($g_{Pd}$). [e] MSA based on linear combination ($\mu$mol/s/$g_{cat}$) = $MSA_{Fe}$ in $Fe_2O_3$ (0.38 $\mu$mol/s/$g_{Fe}$) × Fe loading + $MSA_{Pd}$ in 5Pd/C (2.65 $\mu$mol/s/$g_{Pd}$) × Pd loading.

In contrast, the 5Pd/C catalyst showed higher ring saturation selectivity irrespective of *m*-cresol conversion, indicating that the direct HDO and ring saturation are parallel reactions. The $MSA_{Fe}$ for $Fe_2O_3$ (0.38 $\mu$mol/s/$g_{Fe}$) was much lower than the $MSA_{Pd}$ for 5Pd/C (2.65 $\mu$mol/s/$g_{Pd}$), indicating that Fe is less active than Pd. Interestingly, the $MSA_{Pd}$ for $Pd/Fe_2O_3$ samples were 1−2 orders of magnitude higher than that of monometallic 5Pd/C catalyst if Pd is considered as the only active sites, meaning the extraordinarily high activity of Pd alone seems unlikely. On the other hand, the $MSA_{Fe}$ of $Pd/Fe_2O_3$ calculated assuming Fe is the sole active site showed a less remarkable improvement (ca. 2-fold) compared with the monometallic $Fe_2O_3$ catalyst, proportional to those shown in Figure 6. This indicates that Fe is the major active site as proposed in our prior report.[20] The $MSA_{linear}$ for the $Pd/Fe_2O_3$ samples, calculated by assuming a nonsynergic scenario, is much less than the $MSA_{cat}$ obtained experimentally which further indicates that a synergy exists between Pd and Fe. Moreover, the catalyst with lower Pd loading ($0.1Pd/Fe_2O_3$) showed a higher $MSA_{cat}/MSA_{linear}$ ratio and thus a more pronounced synergy effect, likely due to its higher Pd dispersion and more extended Pd−Fe interfaces.[49,50]

**3.3. Role of Pd in the Synergic Catalysis.** During the HDO reaction, it is essential to maintain the metallic Fe surface since the Fe surface serves as the catalytic site for the activation of phenolic compounds.[20,41] However, the Fe surface is known to be readily oxidized by steam, even under a $H_2$ atmosphere.[51] Dufour et al.[18] reported the effect of cofeeding $H_2O$ on the catalysis of $Fe/SiO_2$ in guaiacol HDO reaction at 400 °C. With cofeeding 5% $H_2O$ in a 50% $H_2$ flow, the $Fe/SiO_2$ catalyst was fully oxidized under the reaction conditions and showed no activity in the HDO of guaiacol. As $H_2O$ is an unavoidable product in the HDO reaction and an abundant component in pyrolysis bio-oils, the stability of the Fe surface under the reaction conditions, as well as the potential impact of Pd on the stability of metallic Fe, would be of great importance in the synergic catalysis.

In our recent report,[39] the Pd facilitated reduction of Fe oxide was evident based on $H_2$-TPR studies and DFT calculations, and we proposed the stabilization of metallic Fe via interaction with Pd based on the DFT calculations. To confirm this hypothesis, $H_2$ TPR-MS of the steam treated $1Pd/Fe_2O_3$ and $Fe_2O_3$ catalysts were investigated, and the reversed $H_2$ TPR-MS profiles are shown in Figure 7. Here, both samples were prereduced at 300 °C before being subjected to steam treatment at 300 °C. The distinct peak centered at ca. 240 °C for the $Fe_2O_3$ sample clearly indicates the oxidation of metallic Fe during the steam treatment, while the absence of the reduction peak in the profile for the $1Pd/Fe_2O_3$ suggests that the Pd prevents the metallic Fe from being oxidized during the steam treatment.

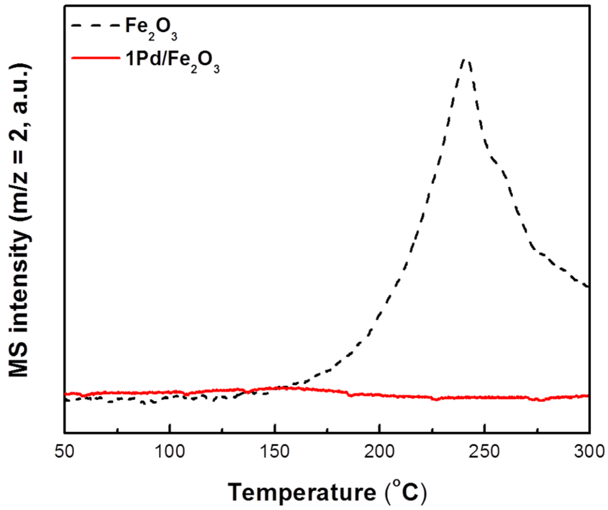

**Figure 7.** $H_2$-TPR-MS profiles for for $1Pd/Fe_2O_3$ and $Fe_2O_3$ samples (signal has been reversed) which were first reduced at 300 °C (ramp rate = 5 °C/min) for 2 h (under 50 vol % $H_2$, 50 mL/min, STP, balanced with He) and then subjected to *in situ* steam treatment at 300 °C for 2 h (under 2.3 vol % $H_2O$, 50 mL/min, STP, balanced with 50 vol % $H_2$ in He).

The resistance to oxidation of metallic Fe in the presence of Pd was also evident in the *in situ* XANES spectra at the Fe K edge for the $1Pd/Fe_2O_3$ sample (Figure 8). The fresh $1Pd/Fe_2O_3$ sample shows the characteristic absorption band for $Fe_2O_3$, while metallic Fe dominates after reduction at 300 °C, evidenced by the resembled feature of the reduced sample with the Fe foil standard. After exposure to steam (ca. 2.3 vol % $H_2O$ with 50 vol % $H_2$, balanced with He), the metallic Fe characteristics in the reduced $1Pd/Fe_2O_3$ were well maintained, indicating the superior stability of $1Pd/Fe_2O_3$ under steam conditions. The stabilization effect introduced by Pd can be attributed to its electronic interaction with the surface Fe atoms.[39]

Such electronic interaction could also facilitate the adsorption behavior on Fe. Our previous DFT studies showed that the interaction between benzene and Fe is remarkably weakened by the addition of Pd.[41] In the HDO of *m*-cresol, a similar phenomenon could also be involved contributing to notable impacts on the synergic catalysis (Figure 6). To confirm this hypothesis, the desorption behavior of toluene, a major product in HDO of *m*-cresol, was investigated with TPD-MS. Figure 9 shows the toluene desorption curves for reduced $1Pd/Fe_2O_3$ and $Fe_2O_3$ samples. The Pd−Fe sample showed a small peak of toluene desorption at a lower temperature of 475

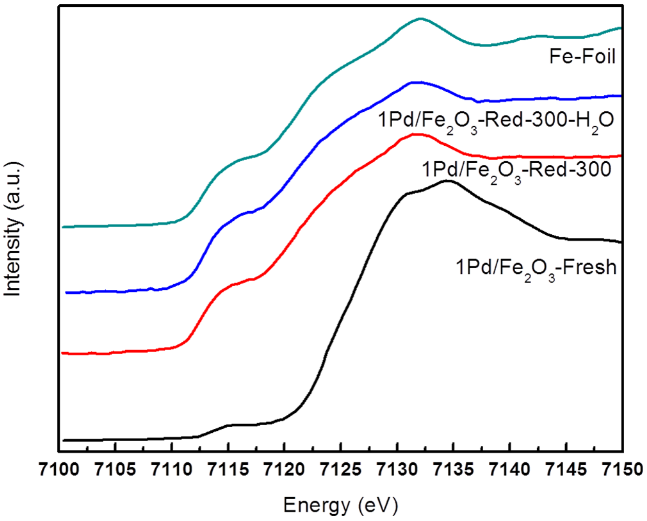

**Figure 8.** *In situ* XANES spectra for fresh, reduced (under 50 vol % $H_2$ (50 mL/min, STP, balanced with Ar) at 300 °C (ramping rate = 5 °C/min) for 2 h) and steam treated (under 2.3 vol % $H_2O$ (50 mL/min, STP, balanced with 50 vol % $H_2$ in Ar) at 300 °C for 30 min after reduction) 1Pd/$Fe_2O_3$ samples with Fe foil reference recorded at Fe K edge.

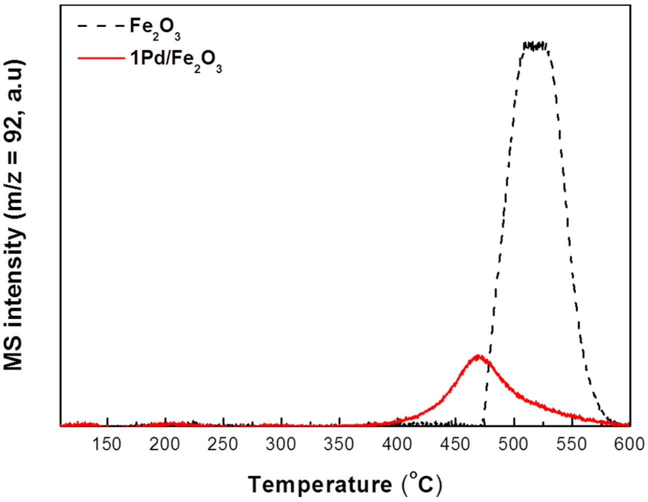

**Figure 9.** Toluene TPD-MS profiles for 1Pd/$Fe_2O_3$ and $Fe_2O_3$ samples which were first reduced at 300 °C (ramp rate = 5 °C/min) for 2 h (under 50 vol % $H_2$, 50 mL/min, STP, balanced with He), then purged with He (50 mL/min, STP) at 400 °C for 30 min, followed by toluene adsorption (under 5.0 vol % toluene, 50 mL/min, STP, balanced with He) at 110 °C for 30 min.

°C, while the desorption peak of toluene on the Fe surface was centered at 525 °C. The lower desorption temperature of toluene on Pd−Fe suggested a weakened toluene−Fe interaction. In addition, the chemisorbed $H_2$ during the reduction process was removed before the TPD tests by purging the reduced catalyst in He at 400 °C. It was found that there is negligible adsorption of toluene without this procedure, suggesting the competitive adsorption between $H_2$ and toluene.

As the chemisorbed $H_2$ is essential in the HDO reaction and has potential impact on the surface redox property as well as the status of other surface species such as aromatic products, it is of interest to reveal the potential impact of Pd on the chemisorption of $H_2$. In our study, the $H_2$ chemisorption was investigated using $H_2$-TPD-MS. Figure 10 shows the $H_2$-TPD-MS profiles for reduced 1Pd/$Fe_2O_3$ and $Fe_2O_3$ samples. For the Fe catalyst, the desorption peaks centered at 250 and 400 °C, while a broader peak from 50−450 °C was observed on the Pd−Fe catalyst. The peaks at 250 and 400 °C suggest the existence of different active sites on the Fe surface, which is related to the heterogeneity of the Fe surface, as indicated in previous reports.[52,53] The lower desorption temperature indicates that the activation of $H_2$ on the Pd−Fe surface has a lower barrier, while the larger area of the desorption peak (by a factor of 2, compared with that of Fe sample) for the Pd−Fe sample indicates the larger population of H adspecies.

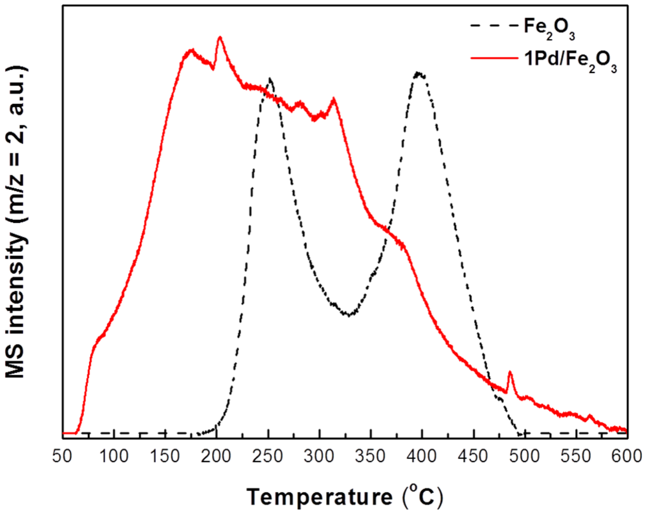

**Figure 10.** $H_2$ TPD-MS profiles for 1Pd/$Fe_2O_3$ and $Fe_2O_3$ samples which were first reduced at 300 °C (ramp rate = 5 °C/min) for 2 h (under 50 vol % $H_2$, 50 mL/min, STP, balanced with He), then purged with He (50 mL/min, STP) at room temperature for 30 min, followed by $H_2$ adsorption (under 50 vol % $H_2$, 50 mL/min, STP, balanced with He) at room temperature for 30 min.

Corma et al.,[54−56] Xu et al.[49,50] and Wong et al.[57,58] reported similar Pt-on-Au and Pd-on-Au catalytic structure for selective hydrogenation. The selectivity of those Pt-on-Au catalysts resembled those for Au in selective hydrogenation of nitro group[54−56] and unsaturated carbonyl compounds.[44,45] In other words, the selectivity characteristics of Au were well-maintained after doping the surface with a noble metal. The role of Au was proposed to be the catalytic sites for the adsorption/activation of substrates, and the precious metals were responsible for $H_2$ activation, as suggested by systematic kinetic studies as well as DFT calculations. One of the major differences between the Pd-on-Au and Pd-on-Fe structures in hydrogenation reactions is the inertness of Au for $H_2$ dissociation[59] vs Fe as an active hydrogenation catalyst.[60] However, a similar argument can still be applied to the Pd-on-Fe system. Keane and Shin[61] found the reaction order with respect to $H_2$ increases with reaction temperatures for phenol HDO over a Ni catalyst and proposed that the surface population of catalytically active $H_2$ is essential for overall catalyst activity. Moreover, the Pt group metals (Pt, Pd, Ru, Rh) show 2−3 orders of magnitude higher sticking probabilities than the Fe group metals (Fe, Ni, Co),[62,63] suggesting a larger population of active hydrogen on the Pd-on-Fe surface compared with the monometallic Fe surface. The activated hydrogen species on Pd can spill over and migrate onto the Fe surface, in a similar manner with Pd doped Cu surface.[64]

The spill over process was also predicted in our DFT calculation. The adsorption of a single hydrogen atom on the Fe (110) surface with a single Pd atom was studied for several different sites: directly atop the Pd impurity (first), directly atop three adjacent Fe atoms with varying Pd−H distances (second, fourth, and fifth), in a long bridge site between the Pd impurity and a nearby Fe atom (third), and in a long bridge site between two Fe atoms near the Pd impurity (sixth). The initial and final structures for adsorbed hydrogen are shown in Figure 11 and the reported adsorption energies were calculated from the total energy of the final hydrogen surface structures. The spillover of the H atom from Pd onto the Fe atoms is evident by the increased adsorption strength for hydrogen away from the Pd atom.

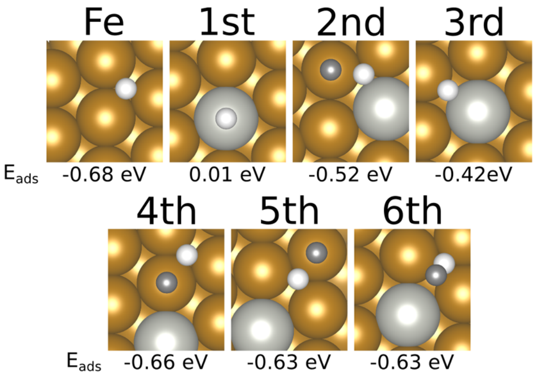

**Figure 11.** Structures examined for the adsorption of a hydrogen adsorption on the Fe (110) (Fe) and Fe (110) with Pd impurity (1st −6th) surfaces. The large gold spheres represent Fe; the large silver spheres represent Pd; the small white spheres represent the final configuration of the hydrogen atom on the surface, and the small gray spheres represent the initial configuration of the hydrogen atom on the surface (e.g., the hydrogen was initially placed at the small gray spheres' location and after optimization had shifted to the small white spheres' location). The adsorption energy is indicated in the table.

To understand whether the synergistic effect between Pd and Fe is ubiquitous to precious metal promoted Fe catalysts, Fe catalysts promoted by other precious metals (Pt, Ru, and Rh) were also studied and compared with Pd−Fe, and the results are shown in Figure 12. Apparently, the addition of a noble metal (Pd, Pt, Ru, and Rh) significantly improves the activity of Fe. Similar to the Pd/$Fe_2O_3$ catalysts, M/$Fe_2O_3$ catalysts (M = Pt, Ru, and Rh) show high selectivity to toluene, with a similar product distribution to that of Fe. The promotion effect of precious metals (Figure 12) can be ranked by the conversion level of *m*-cresol as Pd < Pt < Ru < Rh, which is similar to the order of $H_2$ sticking probability (Pd < Pt < Rh < Ru), further indicating the importance of the $H_2$ sticking capability of the noble metal in promoting the HDO catalysis on Fe. However, the extent of such synergy effects could strongly depend on the dispersion/structure of the noble metals as well as their interaction with Fe.

Recently, Kyriakou et al.[65] reported a similar promotion effect on hydrogen activation by single atom alloys of Pd in bulk Cu (111). The addition of isolated Pd atoms in the Cu (111) surface significantly decreases the $H_2$ desorption temperature in $H_2$-TPD relative to either the clean Cu (111) or Pd (111) surface, similar to the observation reported here (Figure 10). In the PdCu system, the Pd addition provided "entrance" and "exit" routes for the $H_2$ activation and adsorption on the Cu surface, and the hydrogen spillover from the Pd activation site onto the Cu surface was evident with STM observation. Similarly, the active $H_2$ sticking and dissociation site with Pd and the hydrogen spillover onto the Cu surface significantly improves the Cu's activity to perform as a hydrogenating catalyst for styrene and acetylene. Despite the fact that Fe is more capable in $H_2$ activation than Cu, they both have quite low $H_2$ sticking coefficients compared to the noble metals.[62,63] The promotional effect of Pd on both metals appears to be one of the important roles of Pd in the bimetallic catalyst and should be associated with its ability to activate $H_2$ and enrich the surface H population.

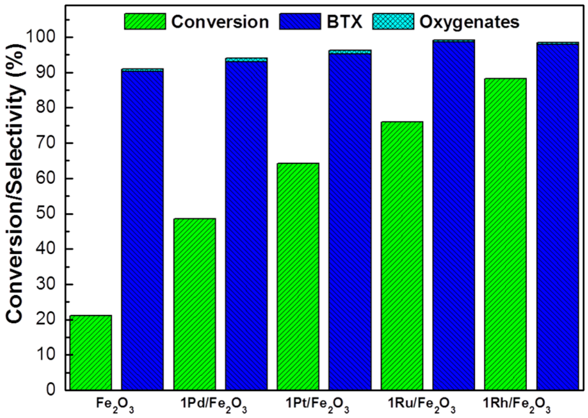

**Figure 12.** Catalytic performances of $Fe_2O_3$ and M/$Fe_2O_3$ (M = Pd, Pt, Ru and Rh) catalysts for *m*-cresol HDO at 300 °C. Catalyst loading = 100 mg; pretreated in flowing 50 vol % $H_2$ (50 mL/min, STP, balanced with $N_2$) at 300 °C (ramp rate = 5 °C/min) for 2 h; reaction gas = 0.45 vol % *m*-cresol and 40 vol % $H_2$, balanced with $N_2$, 40 mL/min (STP); GHSV = 24 000 $h^{-1}$.

On the basis of the discussion above, the mechanism of the Pd−Fe synergic effect can be illustrated with Scheme 2. $H_2$ preferentially adsorbs and dissociates on the Pd entities attached to the Fe surface, followed by spillover to the metallic Fe sites where the substrate, *m*-cresol, adsorbs and activates. The unique adsorption mode of *m*-cresol on the Fe metallic surface enables the high selectivity toward direct HDO products, namely toluene, benzene, and xylene. Meanwhile, Pd is the active site for activating hydrogen and maintains the high hydrogen coverage on the metallic Fe surface as suggested by DFT calculation. Once the product forms via surface reaction on Fe, it readily desorbs to complete the catalytic cycle without further reaction. Another advantage of the surface enrichment of active hydrogen is to efficiently remove the oxygen on the surface and thus suppress the reoxidation of the active Fe under the reaction conditions. In addition, the

**Scheme 2. Mechanism of Pd−Fe Synergy in HDO of *m*-Cresol**

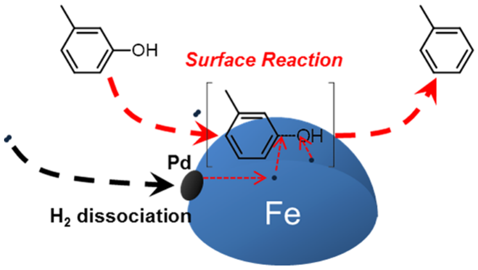

adsorption of aromatics is also modified by the Pd−Fe interaction, leading to a weaker adsorption of desired products.[41] A direct catalytic consequence of such a weakening effect is the facilitated desorption of desired products, mitigating further ring saturation and/or breakdown of products to C1/C2 hydrocarbons.

## 4. CONCLUSIONS

In this work, we report the synergic effect of Pd−Fe in the HDO of lignin derived compounds, i.e., *m*-cresol, and reveal the Pd−Fe structure (Pd entities are present in either 3D clusters and/or 2D flakes on metallic Fe surface) in the reduced Pd/$Fe_2O_3$ catalysts. The addition of Pd was found to facilitate the reduction of Fe under a $H_2$ atmosphere, and the reduced catalysts showed resistance to the surface oxidation of Fe by reactant and water generated during the HDO process. The synergic effect was thus attributed to the Pd facilitated $H_2$ activation, stabilization of metallic Fe by Pd, and Pd promoted product desorption. The synergic effect was also found on other precious metal promoted Fe catalysts, and even more remarkable synergy was found on metals with higher $H_2$ sticking probability.

## ■ ASSOCIATED CONTENT

### Ⓢ Supporting Information

Reaction data obtained at different flow rate and over catalysts with different mesh sizes are added in the Supporting Information, which provides evidence for negligible mass transfer limitation under the reaction conditions used in this research. This material is available free of charge via the Internet at http://pubs.acs.org/.

## ■ AUTHOR INFORMATION

### Corresponding Author

*Phone: 509-371-6273. E-mail: yong.wang@pnnl.gov.

### Notes

The authors declare no competing financial interest.

## ■ ACKNOWLEDGMENTS

We acknowledge the financial support from the U.S. Department of Energy (DOE), Office of Basic Energy Sciences, Division of Chemical Sciences, Geosciences, and Biosciences. This work was also supported by institutional funds provided to J.S.M. from the Voiland School of Chemical Engineering and Bioengineering. We thank the Franceschi Microscopy and Imaging Center (FMIC) at Washington State University for the access to TEM. A portion of the research was performed at Environmental Molecular Sciences Laboratory (EMSL), a national scientific user facility sponsored by the Department of Energy's Office of Biological and Environmental Research and located at Pacific Northwest National Laboratory (PNNL). *In situ* XANES and XRD studies were conducted at the National Synchrotron Light Source at Brookhaven National Laboratory. Use of the National Synchrotron Light Source, Brookhaven National Laboratory, for the XANES experiments was supported by the U.S. Department of Energy, Office of Basic Energy Sciences. Beamline X18A is supported, in part, by the Synchrotron Catalysis Consortium (Grant# DE-FG02-05ER15688). The authors would like to thank Dr. Steve Ehrlich and Dr. Nebojsa Marinkovic for their help and support during the *in situ* XANES and XRD experiments.

## ■ REFERENCES

(1) Huber, G. W.; Iborra, S.; Corma, A. *Chem. Rev.* **2006**, *106* (9), 4044−98.

(2) Chen, H.; Wang, J. X.; Shuai, S. J.; Chen, W. M. *Fuel* **2008**, *87* (15−16), 3462−3468.

(3) Mortensen, P. M.; Grunwaldt, J. D.; Jensen, P. A.; Knudsen, K. G.; Jensen, A. D. *Appl. Catal., A* **2011**, *407* (1−2), 1−19.

(4) Fernando, S.; Adhikari, S.; Chandrapal, C.; Murali, N. *Energy Fuels* **2006**, *20* (4), 1727−1737.

(5) Elliott, D. C. *Energy Fuels* **2007**, *21* (3), 1792−1815.

(6) Demirbas, A. *Appl. Energy* **2011**, *88* (1), 17−28.

(7) Kleinert, M.; Barth, T. *Chem. Eng. Technol.* **2008**, *31* (5), 736−745.

(8) Roberts, V. M.; Stein, V.; Reiner, T.; Lemonidou, A.; Li, X. B.; Lercher, J. A. *Chem.—Eur. J.* **2011**, *17* (21), 5939−5948.

(9) Kordulis, C.; Gouromihou, A.; Lycourghiotis, A.; Papadopoulou, C.; Matralis, H. K. *Appl. Catal.* **1990**, *67* (1), 39−47.

(10) Kabe, T.; Qian, W. H.; Ishihara, A. *J. Phys. Chem.* **1994**, *98* (3), 912−916.

(11) Travert, A.; Nakamura, H.; van Santen, R. A.; Cristol, S.; Paul, J. F.; Payen, E. *J. Am. Chem. Soc.* **2002**, *124* (24), 7084−95.

(12) Laurent, E.; Delmon, B. *J. Catal.* **1994**, *146* (1), 281−291.

(13) Ferrari, M.; Maggi, R.; Delmon, B.; Grange, P. *J. Catal.* **2001**, *198* (1), 47−55.

(14) Viljava, T. R.; Komulainen, R. S.; Krause, A. O. I. *Catal. Today* **2000**, *60* (1−2), 83−92.

(15) Bui, V. N.; Laurenti, D.; Delichere, P.; Geantet, C. *Appl. Catal., B* **2011**, *101* (3−4), 246−255.

(16) Centeno, A.; Laurent, E.; Delmon, B. *J. Catal.* **1995**, *154* (2), 288−298.

(17) Ferrari, M.; Bosmans, S.; Maggi, R.; Delmon, B.; Grange, P. *Catal. Today* **2001**, *65* (2−4), 257−264.

(18) Olcese, R.; Bettahar, M. M.; Malaman, B.; Ghanbaja, J.; Tibavizco, L.; Petitjean, D.; Dufour, A. *Appl. Catal., B* **2013**, *129*, 528−538.

(19) Olcese, R. N.; Bettahar, M.; Petitjean, D.; Malaman, B.; Giovanella, F.; Dufour, A. *Appl. Catal., B* **2012**, *115*, 63−73.

(20) Sun, J.; Karim, A. M.; Zhang, H.; Kovarik, L.; Li, X. S.; Hensley, A. J.; McEwen, J.-S.; Wang, Y. *J. Catal.* **2013**, *306*, 47−57.

(21) Dong, W.; Hafner, J. *Phys. Rev. B* **1997**, *56* (23), 15396.

(22) Ledentu, V.; Dong, W.; Sautet, P. *Surf. Sci.* **1998**, *412−413*, 518−526.

(23) Gutierrez, A.; Kaila, R. K.; Honkela, M. L.; Slioor, R.; Krause, A. O. I. *Catal. Today* **2009**, *147* (3−4), 239−246.

(24) Lin, Y. C.; Li, C. L.; Wan, H. P.; Lee, H. T.; Liu, C. F. *Energy Fuels* **2011**, *25* (3), 890−896.

(25) Olcese, R. N.; Lardier, G.; Bettahar, M.; Ghanbaja, J.; Fontana, S.; Carre, V.; Aubriet, F.; Petitjean, D.; Dufour, A. *ChemSusChem* **2013**, *6* (8), 1490−9.

(26) Olcese, R. N.; Francois, J.; Bettahar, M. M.; Petitjean, D.; Dufour, A. *Energy Fuels* **2013**, *27* (2), 975−984.

(27) Li, S.; Meitzner, G. D.; Iglesia, E. *Stud. Surf. Sci. Catal.* **2001**, *136*, 387−392.

(28) Karim, A. M.; Howard, C.; Roberts, B.; Kovarik, L.; Zhang, L.; King, D. L.; Wang, Y. *ACS Catal.* **2012**, *2* (11), 2387−2394.

(29) Parrish, W.; Mack, M.; Bragg, S. W. H. *Data for X-Ray Analysis*; Centrex Publishing Company: Eindhoven, The Netherlands, 1963; Vol. *1*.

(30) Ravel, B.; Newville, M. *J. Synchrotron Radiat.* **2005**, *12* (4), 537−541.

(31) Newville, M. *J. Synchrotron Radiat.* **2001**, *8* (2), 96−100.

(32) Kresse, G.; Furthmueller, J. *Phys. Rev. B* **1996**, *54* (16), 11169−11186.

(33) Kresse, G.; Hafner, J. *Phys. Rev. B* **1993**, *47* (1), 558−561.

(34) Tereshchuk, P.; Da Silva, J. L. F. *J. Phys. Chem. C* **2012**, *116* (46), 24695−24705.

(35) Ruban, A. V.; Skriver, H. L.; Nørskov, J. K. *Phys. Rev. B* **1999**, *59* (24), 15990−16000.

(36) Nilekar, A. U.; Ruban, A. V.; Mavrikakis, M. *Surf. Sci.* **2009**, *603* (1), 91−96.
(37) Vitos, L.; Ruban, A. V.; Skriver, H. L.; Kollar, J. *Surf. Sci.* **1998**, *411* (1−2), 186−202.
(38) Zhong, W.; Overney, G.; Tomanek, D. *Phys. Rev. B* **1993**, *47* (1), 95−99.
(39) Hensley, A. J. R.; Hong, Y. C.; Zhang, R. Q.; Zhang, H.; Sun, J. M.; Wang, Y.; McEwen, J.-S. *ACS Catal.* **2014**, DOI: 10.1021/cs500565e.
(40) Patterson, A. L. *Phys. Rev.* **1939**, *56* (10), 978−982.
(41) Hensley, A. J.; Zhang, R.; Wang, Y.; McEwen, J.-S. *J. Phys. Chem. C* **2013**, *117* (46), 24317−24328.
(42) Felicissimo, M. P.; Martyanov, O. N.; Risse, T.; Freund, H.-J. *Surf. Sci.* **2007**, *601* (10), 2105−2116.
(43) Conner, G. R. *J. Vac. Sci. Technol.* **1978**, *15* (2), 343−347.
(44) Jenks, C. J.; Chang, S. L.; Anderegg, J. W.; Thiel, P. A.; Lynch, D. W. *Phys. Rev. B* **1996**, *54* (9), 6301−6306.
(45) Wu, C. T.; Yu, K. M.; Liao, F.; Young, N.; Nellist, P.; Dent, A.; Kroner, A.; Tsang, S. C. *Nat. Commun.* **2012**, *3*, 1050.
(46) Zhang, S. L.; Zhang, J. R. *Phys. Status Solidi B* **1994**, *182* (2), 421−427.
(47) Zhao, C.; Camaioni, D. M.; Lercher, J. A. *J. Catal.* **2012**, *288*, 92−103.
(48) Zhao, C.; He, J. Y.; Lemonidou, A. A.; Li, X. B.; Lercher, J. A. *J. Catal.* **2011**, *280* (1), 8−16.
(49) Sun, K. Q.; Hong, Y. C.; Zhang, G. R.; Xu, B. Q. *ACS Catal.* **2011**, *1* (10), 1336−1346.
(50) Hong, Y. C.; Sun, K. Q.; Zhang, G. R.; Zhong, R. Y.; Xu, B. Q. *Chem. Commun. (Cambridge, U. K.)* **2011**, *47* (4), 1300−2.
(51) Rau, H. *J. Chem. Thermodyn.* **1972**, *4* (1), 57−64.
(52) Arabczyk, W.; Jasińska, I.; Pelka, R. *Catal. Today* **2011**, *169* (1), 97−101.
(53) Huazhang, L.; Caibo, L.; Xiaonian, L.; Yaqing, C. *Ind. Eng. Chem. Res.* **2003**, *42* (7), 1347−1349.
(54) Serna, P.; Concepcion, P.; Corma, A. *J. Catal.* **2009**, *265* (1), 19−25.
(55) Boronat, M.; Corma, A. *Langmuir* **2010**, *26* (21), 16607−14.
(56) Serna, P.; Boronat, M.; Corma, A. *Top. Catal.* **2011**, *54* (5−7), 439−446.
(57) Nutt, M. O.; Heck, K. N.; Alvarez, P.; Wong, M. S. *Appl. Catal., B* **2006**, *69* (1−2), 115−125.
(58) Nutt, M. O.; Hughes, J. B.; Wong, M. S. *Environ. Sci. Technol.* **2005**, *39* (5), 1346−1353.
(59) Hammer, B.; Norskov, J. K. *Nature* **1995**, *376* (6537), 238−240.
(60) Casey, C. P.; Guan, H. *J. Am. Chem. Soc.* **2007**, *129* (18), 5816−7.
(61) Shin, E. J.; Keane, M. A. *J. Catal.* **1998**, *173* (2), 450−459.
(62) Johansson, M.; Lytken, O.; Chorkendorff, I. *J. Chem. Phys.* **2008**, *128* (3), 034706.
(63) Christmann, K. *Surf. Sci. Rep.* **1988**, *9* (1−3), 1−163.
(64) Ramos, M.; Martinez, A. E.; Busnengo, H. F. *Phys. Chem. Chem. Phys.* **2012**, *14* (1), 303−10.
(65) Kyriakou, G.; Boucher, M. B.; Jewell, A. D.; Lewis, E. A.; Lawton, T. J.; Baber, A. E.; Tierney, H. L.; Flytzani-Stephanopoulos, M.; Sykes, E. C. H. *Science* **2012**, *335* (6073), 1209−1212.